

Understanding Performance Limitations of Cu(In,Ga)Se₂ Solar Cells due to Metastable Defects—A Route toward Higher Efficiencies


Thomas Paul Weiss,* Florian Ehre, Valentina Serrano-Escalante, Taowen Wang, and Susanne Siebentritt

Thin-film Cu(In,Ga)Se₂ solar cells reach power conversion efficiencies exceeding 23% and nonradiative recombination in the bulk is reported to limit device performance. The diode factor has not received much attention, although it limits the fill factor, and therefore the efficiency, for state-of-the-art solar cells. Herein, the diode factor of Cu(In,Ga)Se₂ absorbers, measured by photoluminescence spectroscopy, and of solar cells, measured by current–voltage and capacitance–voltage characteristics, are compared, supported by simulations using rate equations of generation and recombination. It is found that the diode factor is already increased in the neutral zone of the absorber due to metastable defects, such as the V_{Se}–V_{Cu} defect found in Cu(In,Ga)Se₂, because of an increased net acceptor density upon minority-carrier injection. The metastable and persistent increase of the net acceptor density has a detrimental effect on the device performance. Diode factors of 1 and efficiencies exceeding 24% are expected when, in current state-of-the-art Cu(In,Ga)Se₂ solar cells, the formation of metastable defects is suppressed.

1. Introduction

Among the photovoltaic technologies, thin-film solar cells offer the lowest CO₂-equivalent emission per kilowatt hour and are therefore crucial for sustainable and green electricity production.^[1] With an efficiency of 23.35%,^[2] Cu(In,Ga)(S,Se)₂ (CIGS) solar cells reach the highest efficiencies among the thin-film technologies.^[3] The efficiency for these solar cells is limited by nonradiative recombination,^[4] in particular originating from grain boundary recombination,^[5] which limits the open circuit voltage.

Dr. T. P. Weiss, Dr. F. Ehre, V. Serrano-Escalante, T. Wang, Prof. S. Siebentritt
Laboratory for Photovoltaics
Department of Physics and Materials Science Research Unit
University of Luxembourg
L-4422 Belvaux, Luxembourg
E-mail: thomas.weiss@uni.lu

 The ORCID identification number(s) for the author(s) of this article can be found under <https://doi.org/10.1002/solr.202100063>.

© 2021 The Authors. Solar RRL published by Wiley-VCH GmbH. This is an open access article under the terms of the Creative Commons Attribution License, which permits use, distribution and reproduction in any medium, provided the original work is properly cited.

DOI: 10.1002/solr.202100063

Another important parameter is the diode factor, which describes the voltage dependence of the diode current.^[6] A higher diode factor reduces the fill factor (FF) of the current–voltage characteristics and therefore the efficiency of the solar cell. For materials exhibiting good transport properties^[7] and sufficient doping, a p–n junction is preferred over a p–i–n solar cell architecture; ideally, it is dominated by recombination in the quasineutral region and thus a diode factor of 1 is expected.^[8] Although a p–n junction is used in CIGS-based solar cells, even cells exceeding 22% show diode factors of around 1.4.^[9] Analyzing the origin of the diode factor on complete devices is ambiguous due to the complex device stack and intentional composition grading of the absorber.^[10] However, the IV characteristic, and thus the diode factor, of the absorber itself

(without a pn junction) can also be retrieved from excitation-dependent photoluminescence.^[11] Under these circumstances, no space charge region exists and the interpretation is simplified. The technique was recently applied to CIGS,^[12] perovskite,^[13] and CdTe,^[14] where diode factors between 1 and 2 are observed. In the case of lowly doped perovskite, photoluminescence is always conducted in high-injection conditions. Upon generating electron–hole pairs, both quasi-Fermi levels adjust and therefore a diode factor of 2 is expected. The diode factor decreases from 2 due to dominating interface recombination.^[13] In contrast, photoluminescence in p-type CIGS occurs in low-injection conditions and only the electron quasi-Fermi level is expected to move, which would result in a diode factor of 1. However, experiments always show values above 1.^[12] Shockley–Read–Hall recombination^[15,16] in the bulk or at the interface cannot explain the high diode factor; however, it is crucial to improve CIGS efficiencies beyond the state of the art.

Here, we show that the diode factor above 1 is due to an additional shift of the majority-carrier Fermi level upon illumination, even though low-injection conditions prevail. This shift is caused by metastable defects involving large lattice relaxation and a change in dopant character upon illumination. CIGS absorber layers generally show metastable behavior, e.g., the doping density and conductivity increase persistently after minority-carrier injection.^[17–21] The behavior is often assigned to the V_{Se}–V_{Cu}

defect complex.^[22] Although the increased acceptor density (i.e., hole quasi-Fermi level closer to the valence band) has been studied for more than 25 years,^[23] the influence of these metastabilities on the diode factor of the bare absorber (measured optically) and of the solar cell (measured electrically) has not been considered. Identifying and avoiding the formation of metastable defects in solar cell devices will therefore become an important topic for further improvements in solar cell device performance. It is shown that the efficiency of state-of-the-art CIGS solar cells can be increased to 24% if these metastabilities can be avoided.

2. Simulation

2.1. The Optical Diode Factor

The optical diode factor was described and related to the electrical diode factor previously^[12] and is recaptured here. The spectral photoluminescence flux $j_\gamma(E)$ as a function of energy E is given by generalized Planck's law in the Boltzmann approximation^[24]

$$j_\gamma(E) = a(E) \frac{E^2}{4\pi^2 \hbar^3 c^2} \exp\left(-\frac{E - \Delta\mu}{k_B T}\right) \quad (1)$$

resulting in the total photoluminescence yield

$$Y_{PL} = \int_0^\infty dE j_\gamma(E) = C \exp\left(\frac{\Delta\mu}{k_B T}\right) \quad (2)$$

In Equation (1) and (2), $a(E)$ is the absorptance, \hbar the reduced Planck constant, c the vacuum speed of light, k_B the Boltzmann constant, T the temperature, and $\Delta\mu$ the quasi-Fermi-level splitting. The constant C comprises the integral of the energy-dependent terms and the constants in Equation (1). The PL yield is empirically found to follow a power law over many orders of magnitude of excitation intensity

$$Y_{PL} \propto G^{A_{opt}} \quad (3)$$

where G is the generation flux. Combining (2) and (3) gives

$$G = C' \exp\left(\frac{\Delta\mu}{A_{opt} k_B T}\right) \quad (4)$$

with A_{opt} the optical diode factor and C' a constant.

The optical diode factor relates to the electrical diode factor measured by current–voltage characteristics. At open-circuit voltage V_{oc} , the diode equation reads

$$J_{SC} = J_0 \exp\left(\frac{qV_{oc}}{A_{el} k_B T}\right) \quad (5)$$

The prefactor J_0 is the saturation current density, J_{SC} the short-circuit current density, and A_{el} the (electrical) diode factor. Assuming good collection of photogenerated charge,^[7] the short-circuit current equals the generation flux G . The open-circuit voltage V_{oc} is given by the quasi-Fermi-level splitting of the absorber, which is met for CIGS.^[25] Under these circumstances, the optical diode factor A_{opt} equals A_{el} and holds if the recombination process is the same, i.e., in the quasi-neutral region.

From simulations and experiments, the optical diode factor is extracted from an excitation-dependent photoluminescence (PL) measurement rewriting Equation (3) as

$$A_{opt} = \frac{\partial \log Y_{PL}}{\partial \log G} \quad (6)$$

Following Shockley–Read–Hall recombination statistics, the calculated PL yield (Equation (2)) and optical diode factor (Equation (6)) are shown in **Figure 1a** as blue lines for a p-type semiconductor. Details of the calculations are given in the Supporting Information. In low-injection conditions, an increased generation flux increases the minority (electron) Fermi level, whereas the majority (hole) quasi-Fermi level is

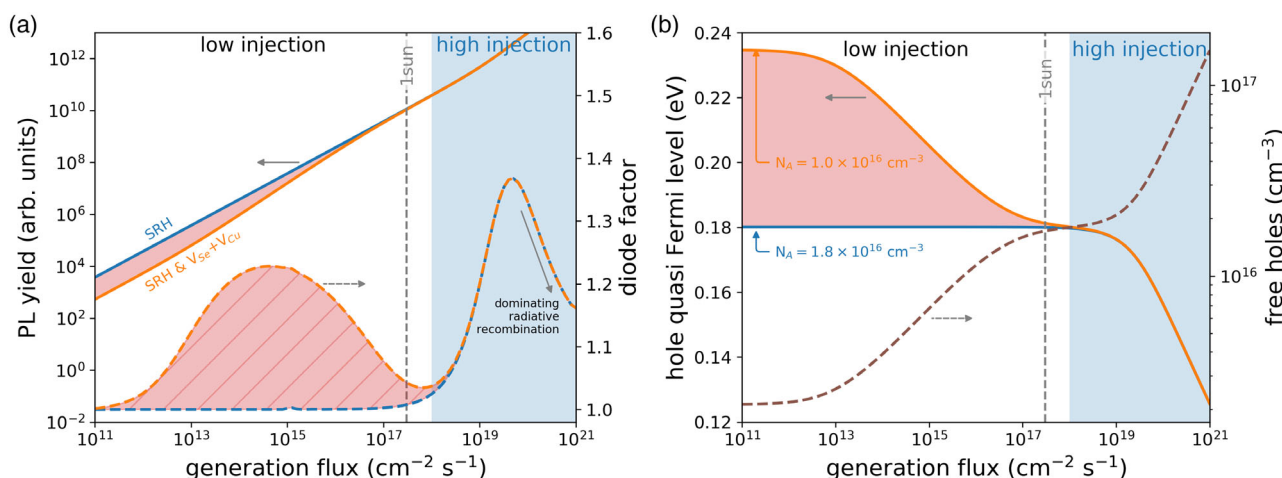


Figure 1. a) PL yield as a function of generation rate for SRH recombination (blue line) and with additional metastable defects (orange line). The diode factor is calculated from the local slope of the PL yield and plotted on the right ordinate (dashed lines). The hatched red area indicates the increased diode factor due to the conversion of metastable donors into acceptors upon illumination. b) Due to the creation of metastable acceptors, an additional downshift of the hole quasi-Fermi level is observed. The valence band is positioned at 0 eV. Evidently, due to the downshift of the hole quasi-Fermi level, the hole density increases (dashed line and right ordinate in (b)). The metastable defect concentration for the V_{Se}–V_{Cu} defect complex is set to $N_{MS} = 8 \times 10^{15} \text{ cm}^{-3}$. Other parameters and details of the calculations can be found in Table 1, 2, and the Supporting Information.

constant. Consequently, a diode factor of 1 is obtained. In contrast, in high injection, in addition the hole quasi-Fermi level decreases, resulting in a diode factor of 2. For generation fluxes above $10^{20} \text{ cm}^{-2} \text{ s}^{-1}$, radiative recombination dominates over Shockley–Read–Hall recombination and therefore the diode factor converges to 1.

2.2. Optical Diode Factors above 1 in Low-Injection Conditions

Experimentally, an optical diode factor >1 is observed for CIGS absorbers in low-injection conditions.^[12] The increased diode factor above 1 in low injection can be explained if the majority-carrier Fermi level shifts toward the respective band edge upon illumination. Experimental evidence for such a shift in CIGS grown in various laboratories is given by an increased net acceptor density upon light soaking measured by capacitance profiling.^[17–20,26] A similar effect is obtained in bare absorber layers by conductivity and Hall measurements confirming the effect resulting from the bulk of the CIGS absorber.^[27,28]

With different net acceptor densities, $N_{A,1}$ and $N_{A,2}$, at different light-generation fluxes $G_1 > G_2$, the (optical) diode factor is expressed as

$$A_{\text{opt}} = A_{\text{opt,SRH}} + \Delta A_{\text{opt}} \quad (7)$$

The first component is the optical diode factor as expected from SRH recombination (Section 2.1). In low-injection conditions, $A_{\text{opt,SRH}}$ equals 1. The second term ΔA_{opt} is due to the increased acceptor density (and thus the additional shift of the hole quasi-Fermi level toward the valence band) and is expressed as

$$\Delta A_{\text{opt}} = \frac{\ln \frac{N_{A,1}}{N_{A,2}}}{\ln \frac{G_1}{G_2}} \quad (8)$$

Figure 2 shows the quasi-Fermi level shifts and the optical diode factors in low-injection conditions upon a certain generation flux of free charge carriers in the cases without (a) and with (b) an additional shift of the hole quasi-Fermi level. Derivations

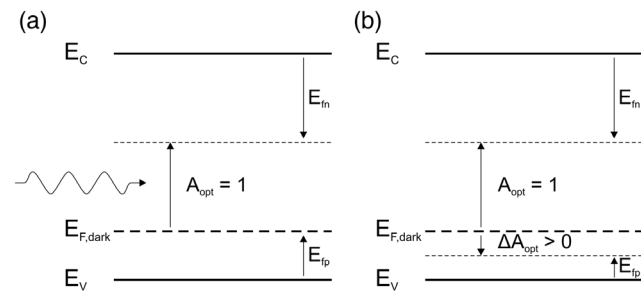


Figure 2. Schematic of a p-type absorber layer under low-injection conditions ($\Delta n \ll p_0$). a) Upon a generation flux (here by photons), the electron quasi-Fermi level E_{fn} moves upward. The obtained quasi-Fermi-level splitting results in an emitted photoluminescence flux of the absorber with a (optical) diode factor of 1. b) Metastable defects result in an increased net acceptor density upon minority-carrier injection. Consequently, and even in low-injection conditions, the majority (hole) quasi-Fermi level E_{fp} shifts toward the valence band. The additional shift increases the diode factor above 1 by ΔA_{opt} .

of Equation (7) and (8) are available in the Supporting Information.

In CIGS, metastable defects, such as the $V_{\text{Se}}-V_{\text{Cu}}$ double vacancy, can explain the experimental results of a diode factor >1 in low-injection conditions: From first-principles calculations, it is found that the $V_{\text{Se}}-V_{\text{Cu}}$ defect can convert from a shallow donor to a shallow acceptor upon capture/emission of free charge carriers, which requires thermal activation.^[22]

The transition between the donor and acceptor state happens upon double emission/capture processes of electrons and holes, involving energy barriers ΔE due to lattice relaxations. Thus, in general, the transition rate τ_{DA}^{-1} between the donor and acceptor state can be expressed as^[26] (see also Supporting Information)

$$\tau_{\text{DA}}^{-1} = \nu_{\text{ph}} \exp\left(-\frac{\Delta E}{k_B T}\right) \prod_{i=1}^2 \frac{\tau_{p,i}^{-1}}{\nu_{\text{ph}}} \quad (9)$$

where ν_{ph} is the phonon frequency and $\tau_{p,i}^{-1}$ the transition rates for single capture/emission events. Equation (9) can be understood as follows: The first term $\nu_{\text{ph}} \exp(-\Delta E/k_B T)$ represents the frequency of a successful activation attempt of the energy barrier, while the factors $\tau_{p,i}^{-1}/\nu_{\text{ph}}$ describe the probability of a single capture/emission event in the time window $1/\nu_{\text{ph}}$.^[22]

Although we use the $V_{\text{Se}}-V_{\text{Cu}}$ model, the implications concluded in the following can equally be applied to any metastable defect, as well as other material systems, that changes the net doping persistently (see Lang and Logan^[29] and references therein).

For the $V_{\text{Se}}-V_{\text{Cu}}$ defect complex, the transition rate from donor to acceptor state happens via the electron-capture (EC) and hole-emission (HE) process, whereas the acceptor-to-donor transition is driven by the hole capture (HC) and electron emission (EE). The individual capture/emission processes and mathematical expressions for these transition rates are summarized in Table 2. Additional information is given in the Supporting Information.

The calculated PL yield (Equation (2)) and optical diode factor (Equation (6)) including metastable defects are plotted in Figure 1a. An additional peak with an optical diode factor >1 is observed when compared to the diode factor calculated using Shockley–Read–Hall statistics only. The peak appears in low-injection conditions ($\Delta n \ll p_0$). With increasing generation flux, the number of excess electrons increases the rate for the electron-capture process, which will dominate at some point over the hole-capture process (Figure S2, Supporting Information). Therefore, metastable defects convert from donor to acceptor configuration, which results in a shift of the hole quasi-Fermi level toward the valence band (Figure 1b). This additional shift of the majority-carrier quasi-Fermi level in low-injection conditions is only present due to metastable defects. Thus, the increase of the quasi-Fermi level splitting is stronger compared to the case without metastable defects, and involves the shift of both quasi-Fermi levels, resulting in an optical diode factor larger than 1, as outlined earlier. For high enough generation fluxes, all metastable defects are converted to the acceptor configuration and the optical diode factor approaches 1 again. For even higher generation fluxes, the optical diode factor increases due to high-injection conditions. The concrete simulation shown in Figure 1 results in a diode factor of ≈ 1.2 over more than two orders of magnitude.

The value of the optical diode factor due to metastable defects depends on how much the hole quasi-Fermi level shifts toward the valence band upon the donor-to-acceptor conversion of the metastable defect, i.e., depends on the ratio of metastable defects to doping acceptors (see Figure S3, Supporting Information). If the densities of metastable defects N_{MS} is much smaller than the fixed acceptor density N_A , i.e. ($N_{MS} \ll N_A$), the hole quasi-Fermi level shifts not significantly and an optical diode factor is close to 1. For $N_{MS} \gg N_A$, the influence of metastable defects becomes significant, resulting in a higher optical diode factor.

The position of the additional peak of the optical diode factor due to metastable defects depends on the values of the energy barriers for the donor-to-acceptor transitions (values for Figure 1 are listed in Table 2). A variation of the energy barrier heights of the two dominant processes (EC and HC) are shown in Figure S2 and S4, Supporting Information. These barriers govern the respective transition rates and consequently the generation flux, where the metastable defect transitions from donor to acceptor. In Figure 1, $\Delta E_{EC} = \Delta E_{HC} = 0.35$ eV, which results in a conversion from donors to acceptors slightly below 1 sun excitation. Similar results are obtained using SCAPS, i.e., including transport and an absorption profile (Figure S5, Supporting Information).

3. Results

3.1. Experimental Determination of the Optical Diode Factor

Figure 3a shows a measurement of the integrated PL yield as a function of the excitation density for two different CIGSe absorbers (see the Experimental Section for more details) exhibiting different optical diode factors. Absorbers were covered with CdS for passivation.^[30–32] From a linear fit (Equation (6)), mean

optical diode factors of 1.15 and 1.36 were extracted in accordance with previous findings of Cu-poor CIGS absorber layers.^[12] In addition, the differential optical diode factor was plotted (Equation (6)). It becomes evident that the sample with a higher mean optical diode factor exhibits an excitation-dependent differential optical diode factor, which is decreasing with increasing excitation intensity (see Figure S6, Supporting Information, for a more detailed investigation). The finding is in agreement with the model of metastable defects (see Section 2.1), which cause an excitation-dependent optical diode factor >1 in low-excitation conditions.

Figure 3b shows apparent doping densities n_{CV} in the equilibrium state and for two different light-soaking intensities (Equation (12)) as measured by capacitance–voltage (CV) measurements. The CV measurements were performed on completed solar cell devices made from absorber layers deposited in the same process run as those used for PL measurements (Figure 3a). Light-soaking exposes the solar cell to illumination, which converts metastable defects from donor to acceptor configuration. The increase in n_{CV} depends on the light intensity (Figure 3b), but not on the light duration (Figure S7, Supporting Information), indicating that the metastable defects reached equilibrium for the light-soaking conditions used here.

According to Equation (7) and (8) (using $A_{opt,SRH} = 1$ for low-injection conditions), the increased hole density results in an optical diode factor of $A_{opt,CV} = 1.20 \pm 0.02$ (Figure 3b) in agreement with the diode factors obtained by PL.

3.2. Impact on IV Characteristics

SCAPS is used for 1D simulations of devices,^[33] including metastable defects.^[26] Simulated IV characteristics, where the

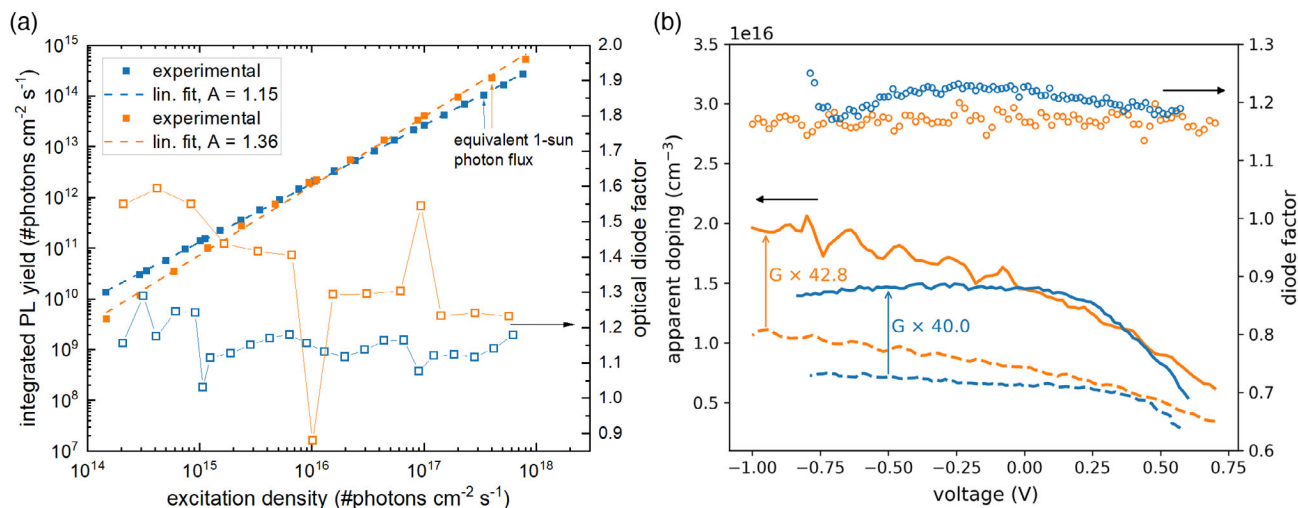


Figure 3. a) Photoluminescence yield with respect to the excitation density (left ordinate). The dashed lines are linear fits from which the mean optical diode factors are extracted (Equation (6)). The differential optical diode factor (right ordinate) shows an excitation-dependent optical diode factor for the sample with the higher mean optical diode factor. b) Apparent doping densities (left ordinate) of the same samples from capacitance–voltage measurements (Equation (12)). Two different light-soaking intensities (corresponding to different generation rates of electron–hole pairs) are used to convert metastable donors to acceptors. From the doping profiles at two different light-soaking intensities, the expected diode factor is calculated using Equation (7) and (8) (right ordinate, open symbols), which agree well with the values obtained from photoluminescence (a). Small differences between these techniques, and also between samples, might arise due to the presence of a space charge region or the necessity to perform the capacitance–voltage measurements at different temperatures (see the Experimental Section and Figure S9, Supporting Information).

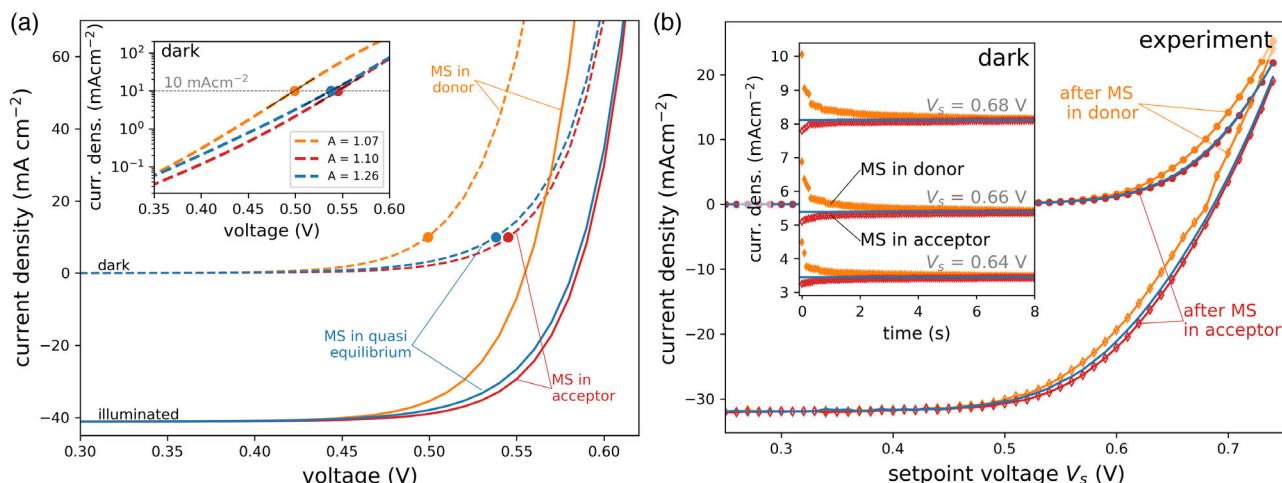


Figure 4. a) Simulated IV characteristics in the dark and under illumination with metastable defects mainly in the donor configuration (yellow curves) and in the acceptor configuration (red curves). The blue curve shows the IV behavior if the metastable defect is in quasi-equilibrium at each voltage point (see also Figure S9a, Supporting Information, for the occupation of the metastable defect with respect to voltage). Inset: dark IV characteristics on a logarithmic ordinate. Solid symbols indicate the voltage V (10 mA cm^{-2}) at a diode current density of 10 mA cm^{-2} . Black dashed lines represent a linear fit in a voltage range of $V(10 \text{ mA cm}^{-2}) \pm 30 \text{ mV}$ to extract the diode factors (see Equation (S33), Supporting Information). Clearly, the diode factor is increased when the metastable defects can follow the voltage sweep, which leads to a reduced FF when compared to the case when the metastable defects are in the acceptor or donor configuration (Figure S10, Supporting Information). b) Impact of metastable defects assessed experimentally. The IV characteristics are constructed by measuring the current density after bringing the metastable defects in the donor or acceptor configuration (see the Experimental Section for details). The quasi-equilibrium current density characteristics are plotted as dashed black lines. Inset: transient behavior of the current density at different voltage set points after bringing the metastable defects in the acceptor and donor configuration. Within a few seconds, the solar cell relaxes to the quasi-equilibrium state.

metastable defects are (mainly) in the donor and acceptor configuration, are shown in **Figure 4a**. The IV curve shifts to higher voltages due to an increased net acceptor density (see band diagram Figure S8, Supporting Information) in agreement with experimental results.^[34] The IV characteristic, where the state of the metastable defects is in quasi-equilibrium with each applied voltage (Figure 9a, Supporting Information), exhibits a clearly reduced FF (blue curve) compared to the curve, where all metastable defects are in the acceptor or donor state (Figure 10, Supporting Information). The reduced FF results from an increased diode factor (inset Figure 4a). It is interesting to note that the increase of the diode factor, where the metastable defect is in quasi-equilibrium compared to the ones with pure acceptor or donor state, is similar to the increase demonstrated by the simulations of the optical diode factor (Section 2.1 and Figure 1).

The same behavior is observed experimentally (Figure 4b), where the IV curve is constructed after bringing the metastable defects in the donor and acceptor configuration. The transient behavior of the current density (Figure 4b inset) shows that the relaxation process to the quasi-equilibrium has a time constant of a few seconds. Although a qualitative agreement is found between experiment and simulation, the finite time resolution imposed experimentally underestimates the difference between the experimental IV curves with metastable defects in the donor and acceptor configuration (orange and red curve in Figure 4b). A better agreement toward the simulation result is expected if the time resolution for the transient IV measurements can be improved. Also, the simulation results are subject to the input parameters. Simulated IV curves with carrier lifetimes reduced by a factor of 3 ($\tau_n = \tau_p = 33 \text{ ns}$)

are shown in Figure S11, Supporting Information, where the IV curve with metastable defects in quasi-equilibrium is rather centered around the two curves with metastable defects in the donor or acceptor configuration.

4. Discussion

4.1. Impact of the Diode Factor on the Efficiency

In the previous two subsections, it was shown that the illumination-dependent acceptor density directly influences the diode factor of the absorber layer (measured optically by PL) and of the solar cell device (measured electrically). **Figure 5** shows calculated IV characteristics with varying diode factors using the diode equation

$$J(V) = J_0 \left[\exp\left(\frac{qV - r_s J}{A_{\text{el}} k_B T}\right) - 1 \right] + \frac{qV - r_s J}{R_{\text{sh}}} - J_{\text{sc}} \quad (10)$$

which is similar to Equation (5), but includes a series and shunt resistance r_s and R_{sh} , respectively. The saturation current density J_0 is adjusted for each diode factor such that $V_{\text{OC}} = 0.734 \text{ V}$ and $J_{\text{SC}} = 39.6 \text{ mA cm}^{-2}$ (as reported for the best CIGS solar cell^[2]). Clearly, the diode factor has a significant influence: the FF and thus the efficiency are affected (inset in Figure 5). Reducing the diode factor and therefore increasing the FF would improve the efficiency to $\approx 24\%$ absolute. The results presented here show that metastable defect concentrations need to be reduced to achieve this goal.

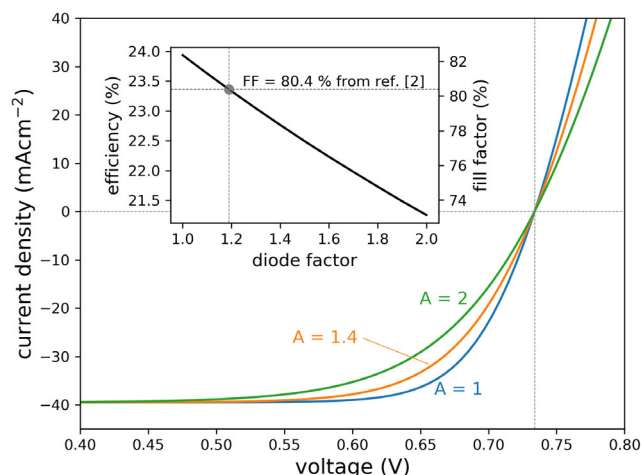


Figure 5. IV characteristics calculated according to Equation (10) for different diode factors. The series and shunt resistances were set to $r_s = 0.5 \Omega \text{ cm}^2$ and $R_{sh} = 5000 \Omega \text{ cm}^2$, respectively. The open circuit voltage (0.734 mV) and short circuit current density (39.6 mA cm^{-2}) are taken from the record device reported elsewhere.^[2] A clear decrease of the FF is observed with an increasing diode factor, resulting in a reduced efficiency (inset). A FF of 80.4% is reported in Nakamura et al.^[2], which can be described by a diode factor of 1.19 and which leads to an efficiency of 23.36% (23.35% reported in Nakamura et al.^[2]).

4.2. The Origin of the Metastable Behavior

Lany and Zunger pointed out that V_{Se} defects will form $V_{Se}-V_{Cu}$ complexes due to a reduction of the total energy.^[22] Therefore, the V_{Se} defects will only exist in the $V_{Se}-V_{Cu}$ complex due to the Cu-poor compositions and therefore the abundance of V_{Cu} defects. Thus, in this work, we investigate CIGS-based absorbers and solar cells, which were intentionally grown with varying Se pressure p_{Se} during growth. Due to the variation of the Se flux, also the integral Cu and Ga content of the CIGS absorber varies, as observed previously.^[35,36] The integral composition is represented by $CGI = [Cu]/([Ga] + [In])$ and $GGI = [Ga]/([Ga] + [In])$.

An increased density of metastable defects increases the optical diode factor (see Figure S3, Supporting Information). However, no correlation of the optical diode factor A_{opt} with respect to p_{Se} and CGI is observed (Figure S11, Supporting Information). The GGI shows a correlation with A_{opt} with the exception of the lowest GGI absorber (Figure S12c, Supporting Information). According to Lany and Zunger, no barrier for electron capture exists for $CuGaSe_2$.^[22] As a result, the conversion of the metastable defect from a donor to acceptor happens at lower excitation densities (Figure S2, Supporting Information). Thus, at excitation densities used to record the PL spectra, most of the defects might already be in the acceptor state and thus, a smaller diode factor is expected with higher Ga content. However, due to the intentional bandgap grading in high-efficiency CIGS absorbers, the PL peak position is more representative for the GGI in the region of dominant recombination.^[25] The plot of A_{opt} versus the PL peak position shows a less pronounced correlation (Figure S12d, Supporting Information). Thus, the origin of metastability in CIGS absorbers

and solar cells is ambiguous and cannot be linked clearly to the $V_{Se}-V_{Cu}$ defect complex.

Recently, it was reported that the Na content of the sample has an influence on the density of metastable defects.^[19,37] However, the samples investigated here show no correlation of the diode factor with the integral Na or K content of the sample (Figure S12e,f, Supporting Information).

5. Conclusion

The diode factor of state-of-the-art CIGS solar cells is above 1 and therefore imposes an efficiency loss due to a reduced FF. We argue that this is a property of the absorber, not the space charge region. We present a novel model that takes into account an additional shift of the majority-carrier Fermi level upon minority-carrier injection in low-excitation conditions, leading to a diode factor above 1. It is shown that metastable defects involving large lattice relaxations can explain this shift. We use the $V_{Se}-V_{Cu}$ defect complex in CIGS solar cells as an example, which changes from a shallow donor to a shallow acceptor upon electron injection. Net doping densities measured by capacitance–voltage measurements corroborate the model: The net acceptor density is increased by illumination. The experimental increase of the net doping density implies a diode factor of ≈ 1.2 , in agreement with values measured optically by photoluminescence spectroscopy. Thus, a direct and detrimental impact of these metastabilities on solar cell performance is demonstrated as the diode factor is increased, as supported by device simulations including metastable defects. Experimentally, time-resolved IV measurements are presented, which show a behavior in accordance to simulations. The calculated IV characteristics predict that the efficiency of state-of-the-art CIGS solar cells can be improved to 24% if the diode factor can be reduced to 1. Therefore, finding the origin and reducing metastable defects is of significant importance for increased efficiency in these kinds of solar cells.

6. Experimental Section

Polycrystalline CIGSe was grown in a molecular beam epitaxy system by a three-stage evaporation process^[38] on Mo-coated soda lime glass substrates. The Cu/III ratio was controlled by the length of the third stage. The Se flux was tuned from low (1×10^{-6} Torr) to high (6×10^{-6} Torr) pressure by controlling the valve opening of the Se cracker source. Except for the lowest Se pressure of 1×10^{-6} Torr, Cu and Ga source temperatures were kept constant with respect to the different process runs. For the sample with a Se pressure of 1×10^{-6} Torr, the Ga source temperature was decreased to compensate for the lower Cu incorporation.^[35,39] All samples were grown with a final Cu-poor composition ($0.82 < Cu/III < 0.94$).

As-grown samples were etched in 5% aqueous KCN solution for 30 s to remove residual oxides. In a double-jacketed glass reactor, absorbers were then preheated at 67 °C for 3 min in a solution of cadmium sulfate hydrate (2 mM), 28% aqueous ammonium hydroxide (1.5 M), and deionized water. Thiourea (50 mM) was then added to the solution and the reaction was stopped when the solution turned to a turbid yellowish color by affording a 50 nm CdS buffer layer.

Photoluminescence (PL) characterization was conducted on CIGSe absorbers. The absorbers were covered with an ≈ 50 nm CdS layer to prevent degradation during measurements.^[30–32] The samples were excited with a 660 nm diode laser and the PL emission signal was measured by an InGaAs detector array. The measured PL signal was spectrally corrected by measuring the spectrum of a reference lamp. The integrated PL

yield was then obtained by integration of the PL emission flux over the energy from 0.9 to 1.3 eV, which covers the band-to-band transition at room temperature. The excitation flux was calibrated by a power meter, using the beam profile measured with a camera.

Intensity-dependent PL measurements were obtained by tuning the laser power density at the sample surface from 17.5 to 133.3 mW cm⁻². With the addition of neutral density filters, the laser power density was reduced as low as 0.02 mW cm⁻².

Elemental compositions of the CIGSe films were determined by energy-dispersive X-ray spectroscopy with 20 keV acceleration voltage. Elemental standards were used for calibration.

Secondary ion mass spectroscopy was used to determine compositional profiles on bare absorber layers. The samples were bombarded with Cs ions at 1 keV and 15 nA on an area of 200 × 200 μm². The amount of alkali elements was determined relatively among different samples. The respective alkali profile was integrated from the front to the back. The back side was determined where the Mo signal (back contact layer) decreases by a factor of 5 × 10⁻⁴ from its maximum value.

IV measurements were conducted under simulated AM1.5G spectrum (class AAA solar simulator) in a four-probe configuration. A Si reference cell was used for light intensity calibration.

The effect of metastable defects, as investigated by simulations (see later), was measured experimentally by time-resolved measurements with a temporal resolution of ≈100 ms. To bring the metastable defects in the donor configuration, the solar cell was held at a quiescent voltage V_q = 0 V for a duration of 30 s. Subsequently, the time-resolved current density J_s of the solar cell was measured at a set-point voltage V_s for a duration of 30 s. The procedure was repeated for each V_s so that finally

the IV characteristics were constructed from data points of (V_s, J_s). Figure S7b, Supporting Information, exemplifies the measurement routine. Metastable defects were brought into the acceptor configuration by injection of minority carriers at a quiescent voltage of V_q = 0.75 V for a duration of 30 s (see, for instance, Igalsen and Shock^[40]). IV characteristics in the donor and acceptor configuration were constructed from the first readings of J_s (≈100 ms after V_s was applied). The quasi-equilibrium IV characteristics were constructed from the last reading of J_s (≈30 s after V_s was applied).

The admittance of the full solar cell device was measured in a four-probe configuration in the dark. The capacitance and conductance were extracted assuming a RC parallel equivalent circuit. Full devices were mounted in a closed-cycle He cryostat for temperature-dependent measurements. For light-soaking experiments, the solar cells were illuminated for 30 min (if not state otherwise) at two different light intensities at 300 K using a halogen lamp. For each light intensity, the short-circuit current density J_{sc} was measured and subsequently used as an estimate for the generation rate G = $\frac{1}{e}J_{sc}$, which gives the number of electron-hole pairs generated per centimeter squared per second. This estimate is valid under the assumption of good current collection, which is met for high-efficiency CIGS devices.^[7] One light intensity was chosen such that the solar cell produced the same J_{sc} as measured under the solar simulator. The second light intensity was achieved using a neutral density filter, which reduced J_{sc} roughly by a factor of 40. Light soaking induces a metastably increased net acceptor density in the CIGS absorber layer.^[17–21] To measure the increased net acceptor density without relaxation during the measurement, the sample was cooled down to low temperatures, while the illumination was kept on. At set-point temperature, the illumination was switched off and the capacitance–voltage curve was measured under dark conditions at an AC amplitude of 30 mV and a probing frequency of 100 kHz. Due to the front-contact grid, some part of the solar cell is never exposed to light and therefore remains in the relaxed state even during light soaking. The active-area capacitance C_{AA} was then calculated as (see Supporting Information for additional information)

$$C_{AA} = C_{meas} \times \frac{A_{tot}}{A_{active}} - C_{rel} \times \frac{A_{grid}}{A_{active}} \quad (11)$$

where C_{meas} is the measured capacitance (after light soaking), C_{rel} the capacitance in the relaxed state, A_{tot} the total area, A_{grid} the area of the grid, and A_{active} = A_{tot} – A_{grid} the active area of the solar cell.

From the active area capacitance, the apparent net doping density n_{CV} is extracted following^[41]

$$n_{CV}(V) = -\frac{2}{q\epsilon_0\epsilon_R} \left(\frac{d}{dV} \frac{1}{C_{AA}^2} \right)^{-1} \quad (12)$$

where q is the elemental charge, ε₀ and ε_R are the vacuum and material permittivity, and V is the applied bias voltage. Due to the complexity of evaluating the doping density from a capacitance voltage measurement,^[42,43] the error of A_{opt, CV} was determined by the standard deviation of the diode factors evaluated at different bias voltages. Nevertheless, the

Table 1. CIGS material parameters used for simulations.

Name	Symbol	Value
Bandgap	E _g	1.004 eV
Thickness	d	3 μm
Electron affinity	X _{CIGS}	4.3 eV
Dielectric permittivity	ε _R	12
Effective density of states in the conduction band	N _C	7.78 × 10 ¹⁷ cm ⁻³
Effective density of states in the valence band	N _V	2.10 × 10 ¹⁹ cm ⁻³
Electron thermal velocity	v _{th,e}	10 ⁷ cm s ⁻¹
Hole thermal velocity	v _{th,h}	10 ⁷ cm s ⁻¹
Electron mobility	μ _e	10 ² cm ² V ⁻¹ s ⁻¹
Hole mobility	μ _h	25 cm ² V ⁻¹ s ⁻¹
Shallow acceptor density	N _A	10 ¹⁶ cm ⁻³
Metastable defect density	N _{MS}	8 × 10 ¹⁵ cm ⁻³
Electron and hole lifetime	τ _n = τ _p	100 ns
SRH defect level	E _t	Midgap

Table 2. Expression for the four dominating processes to calculate the occupation of the metastable V_{Se} – V_{Cu} defect complex. Detailed derivations can be found in the Supporting Information. The energy barriers are values that are used for the calculation shown in Figure 1. The factors c_n and c_p are the capture constants given by c_n = ν_{th,e}σ_n and c_p = ν_{th,h}σ_h.

Name	Individual capture/emission processes	Expression	Energy barrier	Type
'Electron capture'	Electron capture + hole emission	$\tau_{EC}^{-1} = \frac{1}{\nu_{ph}} c_n c_p n N_V \exp\left(-\frac{\Delta E_{EC}}{k_B T}\right)$	ΔE _{EC} = 0.35 eV	Donor to acceptor
'Hole emission'	Double hole emission	$\tau_{HE}^{-1} = \frac{1}{\nu_{ph}} c_p^2 N_V^2 \exp\left(-\frac{\Delta E_{HE}}{k_B T}\right)$	ΔE _{HE} = 0.76 eV	Donor to acceptor
'Hole capture'	Double hole capture	$\tau_{HC}^{-1} = \frac{1}{\nu_{ph}} c_p^2 p^2 \exp\left(-\frac{\Delta E_{HC}}{k_B T}\right)$	ΔE _{HC} = 0.35 eV	Acceptor to donor
'Electron emission'	Electron emission + hole capture	$\tau_{EE}^{-1} = \frac{1}{\nu_{ph}} c_n c_p p N_C \exp\left(-\frac{\Delta E_{EE}}{k_B T}\right)$	ΔE _{EE} = 0.94 eV	Acceptor to donor

evaluated apparent doping density agrees reasonably well to the doping density in the CIGSe absorber.^[17]

The set-point temperature was chosen such that the capacitance was in a plateau with respect to frequency and temperature and below the N1 capacitance step, as shown in Figure S13, Supporting Information.

SCAPS^[33] is used for 1D simulations of devices and absorbers, including metastable defects.^[26] The same parameters were used as for the calculations conducted in Section 2. Additional parameters are summarized in Table 1. A metastable defect was introduced resembling the $V_{Se}-V_{Cu}$ defect complex with the energy barriers listed in Table 2. In SCAPS, the equilibrium occupation probability of metastable defects $f_{MS,acc}$ (fraction of metastable defects in the acceptor configuration) was determined before an IV simulation and remained constant throughout. $f_{MS,acc}$ was calculated for a given applied voltage V_q (quiescent voltage) and illumination condition. For illuminated IV curves, $f_{MS,acc}$ was also calculated under illumination, whereas for dark IV curves, $f_{MS,acc}$ was calculated in the dark

Supporting Information

Supporting Information is available from the Wiley Online Library or from the author.

Acknowledgements

The authors acknowledge Fonds National de Recherche in Luxembourg for partially funding this research through the SeVac (C17/MS/11655733/SeVaC) and PACE (PRIDE 17/12246511/PACE) project. The authors greatly acknowledge Thomas Schuler for technical assistance and Michele Melchiorre for invaluable support in solar cell finishing.

Conflict of interest

The authors declare no conflict of interest.

Data Availability Statement

The data that support the findings of this study are available from the corresponding author upon reasonable request.

Keywords

chalcopyrites, diode factors, efficiencies, metastable defects, persistent photoconductivity, solar cells, thin films

Received: February 1, 2021

Revised: March 8, 2021

Published online:

- [1] E. G. Hertwich, J. Aloisi de Lardere, A. Arvesen, P. Bayer, J. Bergerson, E. Bouman, T. Gibon, G. Heath, C. Peña, P. Purohit, A. Ramirez, S. Suh, *Green Energy Choices: The Benefits, Risks and Trade-Offs of Low-Carbon Technologies for Electricity Production*, UNEP, Paris **2016**.
- [2] M. Nakamura, K. Yamaguchi, Y. Kimoto, Y. Yasaki, T. Kato, H. Sugimoto, *IEEE J. Photovoltaics* **2019**, *9*, 1863.
- [3] M. A. Green, E. D. Dunlop, J. Hohl-Ebinger, M. Yoshita, N. Kopidakis, X. Hao, *Prog. Photovoltaics* **2020**, *28*, 629.
- [4] S. Siebentritt, E. Avancini, M. Bär, J. Bombsch, E. Bourgeois, S. Buecheler, R. Carron, C. Castro, S. Duguay, R. Félix, E. Handick, D. Hariskos, V. Havu, P. Jackson, H. P. Komsa, T. Kunze, M. Malitckaya, R. Menozzi, M. Nesladek, N. Nicoara, M. Puska, M. Raghuvanshi, P. Pareige, S. Sadewasser, G. Sozzi, A. N. Tiwari, S. Ueda, A. Vilalta-Clemente, T. P. Weiss, F. Werner, R. G. Wilks, W. Witte, M. H. Wolter, *Adv. Energy Mater.* **2020**, *10*, 1903752.
- [5] M. Krause, A. Nikolaeva, M. Maiberg, P. Jackson, D. Hariskos, W. Witte, J. A. Márquez, S. Levchenko, T. Unold, R. Scheer, D. Abou-Ras, *Nat. Commun.* **2020**, *11*, 4189.
- [6] R. Scheer, H. W. Schock, *Chalcogenide Photovoltaics: Physics, Technologies, and Thin Film Devices*, Wiley-VCH Verlag & Co. KGaA, Weinheim, Germany **2011**.
- [7] R. Carron, E. Avancini, T. Feuer, B. Bissig, P. A. Losio, R. Figi, C. Schreiner, M. Bürki, E. Bourgeois, Z. Remes, M. Nesladek, S. Buecheler, A. N. Tiwari, *Sci. Technol. Adv. Mater.* **2018**, *19*, 396.
- [8] T. Kirchartz, U. Rau, *Adv. Energy Mater.* **2018**, *8*, 1703385.
- [9] P. Jackson, R. Wuerz, D. Hariskos, E. Lotter, W. Witte, M. Powalla, *Phys. Status Solidi RRL* **2016**, *10*, 583.
- [10] T. Orgis, M. Maiberg, R. Scheer, *J. Appl. Phys.* **2013**, *114*, 214506-1.
- [11] T. Trupke, R. A. Bardos, M. D. Abbott, J. E. Cotter, *Appl. Phys. Lett.* **2005**, *87*, 093503.
- [12] F. Babbe, L. Choubrac, S. Siebentritt, *Sol. RRL* **2018**, *2*, 1800248.
- [13] P. Caprioglio, C. M. Wolff, O. J. Sandberg, A. Armin, B. Rech, S. Albrecht, D. Neher, M. Stollerfoht, *Adv. Energy Mater.* **2020**, *10*, 2000502.
- [14] D. Kuciauskas, J. Moseley, P. Ščejev, D. Albin, *Phys. Status Solidi RRL* **2020**, *14*, 1900606.
- [15] W. Shockley, W. T. Read, *Phys. Rev.* **1952**, *87*, 835.
- [16] R. N. Hall, *Phys. Rev.* **1952**, *87*, 387.
- [17] J. Bailey, G. Zapalac, D. Poplavskyy, in *Conf. Record of the IEEE Photovoltaic Specialists Conf.*, IEEE, Piscataway, NJ **2016**.
- [18] T. Eisenbarth, R. Caballero, M. Nichterwitz, C. A. Kaufmann, H. W. Schock, T. Unold, *J. Appl. Phys.* **2011**, *110*, 094506.
- [19] M. Igalson, M. Maciaszek, K. Macielak, A. Czudek, M. Edoff, N. Barreau, *Thin Solid Films* **2019**, *669*, 600.
- [20] T. P. Weiss, S. Nishiwaki, B. Bissig, S. Buecheler, A. N. Tiwari, *Phys. Chem. Chem. Phys.* **2017**, *19*, 30410.
- [21] U. Rau, K. Weinert, Q. Nguyen, M. Mamor, G. Hanna, A. Jasenek, H. W. Schock, *MRS Proc.* **2001**, *668*, H9.1.
- [22] S. Lany, A. Zunger, *J. Appl. Phys.* **2006**, *100*, 113725.
- [23] M. Igalson, *Phys. Status Solidi A* **1993**, *139*, 481.
- [24] P. Wurfel, *J. Phys. C: Solid State Phys.* **1982**, *15*, 3967.
- [25] M. H. Wolter, B. Bissig, E. Avancini, R. Carron, S. Buecheler, P. Jackson, S. Siebentritt, *IEEE J. Photovoltaics* **2018**, *8*, 1320.
- [26] K. Decock, P. Zabierowski, M. Burgelman, *J. Appl. Phys.* **2012**, *111*, 043703.
- [27] U. Rau, M. Schmitt, J. Parisi, W. Riedl, F. Karg, *Appl. Phys. Lett.* **1998**, *73*, 223.
- [28] T. Meyer, F. Engelhardt, J. Parisi, U. Rau, *J. Appl. Phys.* **2002**, *91*, 5093.
- [29] D. V. Lang, R. A. Logan, *Phys. Rev. Lett.* **1977**, *39*, 635.
- [30] D. Regesch, L. Gütay, J. K. Larsen, V. Deprédurand, D. Tanaka, Y. Aida, S. Siebentritt, *Appl. Phys. Lett.* **2012**, *101*, 112108.
- [31] W. K. Metzger, I. L. Repins, M. Romero, P. Dippo, M. Contreras, R. Noufi, D. Levi, *Thin Solid Films* **2009**, *517*, 2360.
- [32] F. Babbe, L. Choubrac, S. Siebentritt, *Appl. Phys. Lett.* **2016**, *109*, 082105.
- [33] M. Burgelman, P. Nollet, S. Degraeve, *Thin Solid Films* **2000**, *361*, 527.
- [34] F. Obereigner, N. Barreau, W. Witte, R. Scheer, *J. Appl. Phys.* **2015**, *117*, 055704.
- [35] V. Deprédurand, T. Bertram, S. Siebentritt, *Phys. B: Condens. Matter* **2014**, *439*, 101.
- [36] H. Kempa, T. Rissom, U. Hlawatsch, M. Gaudig, F. Obereigner, C. A. Kaufmann, R. Scheer, *Thin Solid Films* **2013**, *535*, 340.
- [37] A. Czudek, A. Urbaniak, A. Eslam, R. Wuerz, M. Igalson, *IEEE J. Photovoltaics* **2020**, *10*, 1926.
- [38] A. M. Gabor, J. R. Tuttle, D. S. Albin, M. A. Contreras, R. Noufi, A. M. Hermann, *Appl. Phys. Lett.* **1994**, *65*, 198.

- [39] T. Sakurai, M. M. Islam, H. Uehigashi, S. Ishizuka, A. Yamada, K. Matsubara, S. Niki, K. Akimoto, *Sol. Energy Mater. Sol. Cells* **2011**, 95, 227.
- [40] M. Igalson, H. W. Schock, *J. Appl. Phys.* **1996**, 80, 5765.
- [41] S. Sze, K. K. Ng, *Physics of Semiconductor Devices*, 3rd ed., John Wiley & Sons, Inc., Hoboken, NJ, USA **2006**.
- [42] G. Sozzi, M. Lazzarini, R. Menozzi, R. Carron, E. Avancini, B. Bissig, S. Buecheler, and A. N. Tiwari, in *Conf. Record of the IEEE Photovoltaic Specialists Conf.*, IEEE, Piscataway, NJ **2016**.
- [43] A. Niemegeers, M. Burgelman, in *Conf. Record of the IEEE Photovoltaic Specialists Conf.*, IEEE, Piscataway, NJ **1996**.